Systematic design of tetra-petals auxetic structures with stiffness constraint

Zhen-Pei Wang[a], Leong Hien Poh[a,*], Yilin Zhu[a,b], Justin Dirrenberger[c], Samuel Forest[d]

[a]Department of Civil and Environmental Engineering, National University of Singapore, 1 Engineering Drive 2, E1A 07-03, Singapore 117576, Singapore
[b]School of Civil Engineering and Architecture, Southwest Petroleum University, Chengdu 610500, China
[c]Laboratoire PIMM, Arts et Métiers-ParisTech, Cnam, CNRS, 151 bd de l'Hôpital, Paris 75013, France
[d]Centre des Matériaux, Mines ParisTech, CNRS UMR 7633, PSL Research University, Evry Cedex BP 8791003, France

HIGHLIGHTS

- NURBS parameterization of novel curved tetra-petals auxetics
- Isogeometric analysis enhanced numerical homogenization framework.
- A systematical study of designing tetra-petals auxetics with tunable properties
- Bounding graph of achievable effective Poisson's ratio under different stiffness constraints
- Experimental verifications for tunable design studies

GRAPHICAL ABSTRACT

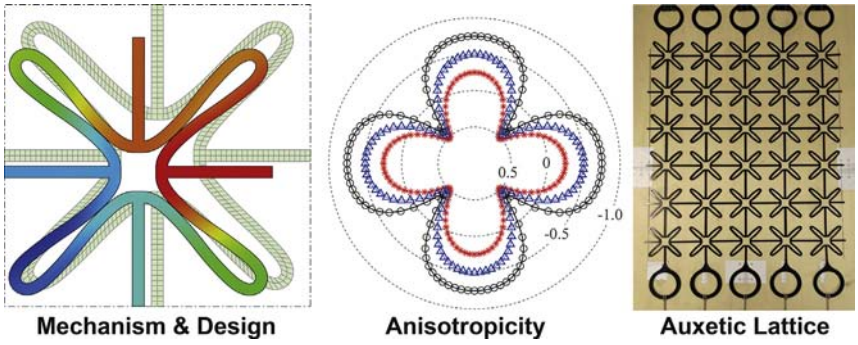

ARTICLE INFO

Article history:
Received 29 October 2018
Received in revised form 12 January 2019
Accepted 19 February 2019
Available online 6 March 2019

Keywords:
Negative Poisson's ratio
Petal auxetic
Computational homogenization
Shape form optimization
Isogeometric analysis

ABSTRACT

This paper focuses on a systematic isogeometric design approach for the optimal petal form and size characterization of tetra-petals auxetics, considering both plane stress and plane strain conditions. The underlying deformation mechanism of a tetra-petals auxetic is analyzed numerically with respect to several key parameters. Design optimizations are performed systematically to give bounding graphs for the minimum Poisson's ratio achievable with different stiffness constraints. Tunable design studies with targeted effective Poisson's ratio, shear modulus and stiffness are demonstrated. Potential application for functionally graded lattice structures is presented. Numerical and experimental verifications are provided to verify the designs. The out-of-plane buckling phenomenon in tension for thin auxetics with re-entrant features is illustrated experimentally to draw caution to results obtained using plane stress formulations for designing such structures.

1. Introduction

The tetra-petals auxetic structures, proposed recently in the work in Ref. [1], have the following interesting features:

- Compared to the star-shaped auxetics of which the deformation mechanism relies on a hinge and elastic support system, e.g. shown in Fig. 1 (a), the petal-shaped auxetics can be modeled and built as a continuum, hence averting the difficulty of manufacturing and introducing flexible vertexes design space leading to improved auxeticity. This have been briefly presented in Ref. [1], with a focus on numerical techniques for the design of exterior petal boundaries only, without any change in the reference petal form and size, as illustrated in Fig. 1 (b).

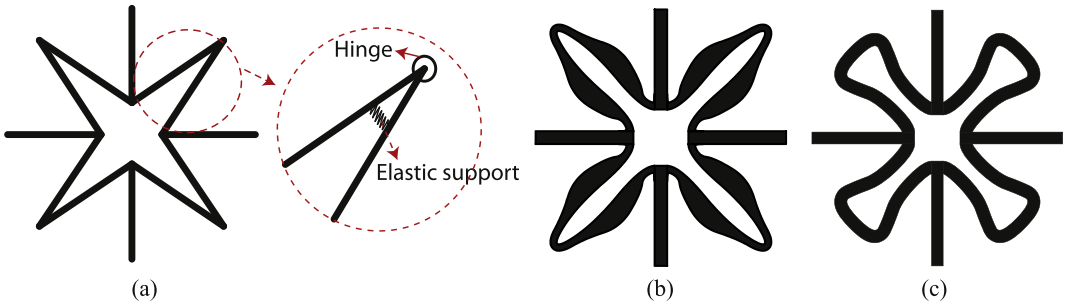

Fig. 1. (a) Star-shaped auxetics and the mechanism at the vertices. The study in Ref. [1] focuses on (b) the design of exterior petal boundary subjected to a geometric width constraint, while the study in this work focus on (c) the optimal shape form and part width of tetra-petals auxetics.

- Compared to the tri- and hexa-petals auxetics that are studied in Ref. [2] with numerical optimization techniques to explore the petal forms and sizes, the tetra-petals auxetics studied in this work generally demonstrate much better auxeticity, which can be tuned by using the same method, as illustrated in Fig. 1 (c). Moreover, as will be demonstrated later, the auxeticity of the tetra-petals auxetics is mainly dependent on the petal form and size, with a negligible influence from the connecting bar size. This feature is attractive for designing wearable electronic skins (e-skins) with tailored local properties, such that the electronic responses and the shape conformance to body joints can be improved, as demonstrated in Refs. [3-5]. The use as e-skins concerns mainly about the negative Poisson's ratio effect and the effective tensile stiffness, for which design studies based on plane stress conditions are mostly adopted.

In this work, the tetra-petals auxetics are systematically studied for both plane stress and plane strain conditions, by exploring the design space of petal form and size. In general, there are two broad approaches for designing such structures ([6]). A common design strategy is to first obtain an in-depth understanding on the interactions between deformation mechanisms of underlying components, to guide the subsequent design of auxetic structures. This was done in the pioneering work of Ref. [7], where an auxetic structure with re-entrant features was designed using rods, hinges and springs. Since then, the auxetic behavior of various structures have been studied intensively, e.g. star-shaped [8,9], chiral [10-13], re-entrant [14-16], rotating polygons/polyhedrons [17,18], star-shaped pores [19] and those with buckling mechanisms [20-22] — see also the details highlighted in recent surveys [23,24]. Potential applications in terms of auxetic nail [25], tubular [26] and energy absorption structures [11,27–30] have also been investigated.

Another broad design strategy is to adopt numerical optimization techniques. This approach is mostly based on topology optimization, e.g. the works of Refs. [31-38], while a few works focus on the structural shape optimization of auxetic structures (e.g. Refs. [1,2,39,40]). Among these works, Wang et al. [1] proposed the smoothed petal-shaped auxetics of which the difficulty of manufacturing hinges and stress concentration induced by sharp corners are significantly reduced, compared to the reference star-shaped auxetics. Following this, the optimal form and size characterization for planar isotropic petal-shaped auxetics, specifically, the tri- and hexa-petals with rotational symmetry, is systematically studied in Ref. [2]. In this paper, we focus on the optimal design of tetra-petals. Departing from Ref. [1], where a fixed petal form was utilized, the framework adopted here follows the form finding strategy in Ref. [2]. Specifically, the petal form and the uniform part width are set as design variables to ensure a larger search space for design purpose.

It should be noted that the design optimization tools used in this work are based on isogeometric analysis (IGA), which adopts non-uniform rational B-spline (NURBS) basis function as the shape function and hence provides significant advantages to perform structure design optimization (see Ref. [41]). Other works using NURBS as a tool for shape optimization can be found in Refs. [42-44].

One aspect of tetra-petals that will be highlighted later is the possible applications as functionally graded lattice structures (e.g., Refs. [45-50]), by focusing on the petal form to achieve the targeted properties. This concept dates back to the work of Ref. [31], and is getting increasing attention for special structural designs with tailored local properties, e.g., recent developments in Refs. [51-60]. In addition to their general lightweight property, the lattice patterns can also demonstrate extraordinary properties, e.g. the recent works in Refs.[11,61,62]. In this work, bounding graphs of achievable negative Poisson's ratio are presented for different stiffness constraints in both plane strain and plane stress conditions, which serve as a guide for designing tetra-petals auxetics with tunable properties. Then, design studies with tunable effective material properties are performed based on the guiding graph. A functionally graded structure made from tetra-auxetic units with same stiffness (same shear and tensile modulus) and varying target effective Poisson's ratios at different locations is presented to demonstrated the potential applications.

The paper is organized as follows: A brief comparison of the star- and petal-shaped auxetics is presented in Section 2. The parameterization method and the mechanisms underlying the auxetic behaviors for tetra-petals structures are discussed in Section 3. A systematic numerical design study for tetra-petals auxetics is given in Section 4. Design studies for unit structures with tunable effective properties and a functionally graded structure made from units with same stiffness yet different effective Poisson's ratios are presented in Section 5, together with numerical verifications of the effective properties. The in-plane anisotropic behavior is also highlighted. Numerical and experimental validations are presented in Section 6, with discussions upon the out-of-plane buckling under tension for re-entrant structures. Finally, some concluding remarks are provided in Section 7.

2. Scope and focus

Star-shaped auxetics, as shown in Fig. 1 (a), is one of the most recognized auxetic structures since [63]. Two important features for the star-shaped auxetics are the re-entrant parts and hinge-functional vertices. In literature, the mechanism underlying star-shaped auxetics has been analyzed by assuming that the re-entrant parts and the vertices are hinges with elastic supports, where each member of the structure is modeled as a rod, e.g., in Refs.[64,65]. It is highlighted that the hinge function and the elastic support are both crucial for the auxetic performance. Without the elastic support, the entire hinge-connected system is unstable. However, such an analysis approach has limited practical usage, due to manufacturing

difficulties in achieving the required stiffness of the stated elastic supports, and the hinge connections at vertices.

The building of star-shaped structures as a continuum model, e.g., the work presented in Ref. [8] is a more accurate description of the actual structure. However, this leads to limited auxetic performance and high stress concentrations [1]. Motivated by the need to reduce stress concentration effect, and to achieve better auxetic performance, petal-shaped auxetics with curved features were proposed in Ref. [1], where the hinge functions and elastic support mechanism are replaced by curved continuum (Fig. 1 (b) and (c)). However, the work in Ref. [1] focused on the design of exterior petal boundary with a fixed petal form (Fig. 1 (b)). In this work, an expanded design space is considered systematically to find the optimal petal form and width for tetra-petal-shaped auxetics, schematically illustrated in Fig. 1, subjected to different stiffness constraints under both plane stress and plane strain conditions. The optimal results form bounding graphs that depict the minimum Poisson's ratio achievable under certain stiffness constraints. Studies with tunable material properties are demonstrated. A functionally graded structure design with different local tetra-petals auxetics is illustrated. Finally, numerical and experimental verifications are performed, and an out-of-plane buckling under tension for re-entrant auxetics under plane stress condition is discussed.

3. Parameterization method and deformation mechanisms

3.1. NURBS-based parameterization

The curved geometry is described using NURBS, with each petal or connecting bar corresponding to one NURBS patch. The NURBS patch describing the petals is characterized in a referential space using 7 design parameters, as depicted in Fig. 2. The interior boundary of the petal is defined with 6 parameters identifying the locations of 10 control points. Variable w_1 defines the location of control point C^1 at the right end of the boundary curve in x_1 direction. The location in x_2 direction is characterized as $h_1 = w_1 \tan(\theta)$, with $\theta = \pi/2$. The location of control point C^2 is defined by moving control point C^1 along the inward direction normal to $\overrightarrow{OC^1}$ by a distance of d_1. Variables w_2, w_3 and w_4 define the locations of control points C^3, C^4 and C^5 in the x_1 direction, respectively. The location of C^5 in the x_2 direction is defined by variable h_4. The locations of C^3 and C^4 in the x_2 direction are set as a linear interpolation between h_1 and h_4, i.e., $h_2 = (h_4 - h_1)/3 + h_1$ and $h_3 = 2(h_4 - h_1)/3 + h_1$. The locations of the control points on the left of the center-line are obtained by mirroring the control points on the right. The exterior boundary of the petal can be identified by offsetting the interior boundary with a width parameter d_2. The petal geometry defined in the referential space is transformed into the physical location to form the petal-shaped auxetics. The width of the connecting bar is characterized with variable d_3, while the length of the connecting bars, l_b, can be identified based on variable w_1 and the unit dimension. The effective properties in the linear regime are non-dimensional. For convenience, we use a dimension of 20 × 20 for each unit. All of the parameter values are normalized based on this dimension, e.g., for an actual unit structure with a dimension 100 × 100, all of the parameters need to be scaled by 5.

To generate the full unit of a tetra-petals auxetic structure, the petal geometry characterized using the above-mentioned parameters is firstly transformed by a distance of $d_4 = \sqrt{2}d_3/2$ along the x_2 direction such that the connecting bars can be placed together with the petal (Fig. 2 (c)). Next, the petals and bars are patterned in a circular fashion to form a full unit structure, as indicated in Fig. 2 (d). If the width of the connecting bars is set to be $d_3 = d_2$, the presented parameterization scheme only require 7 design parameters, i.e., w_i ($i = 1,2,3,4$), h_4 and d_i ($i = 1,2$), to characterize the tetra-petals structures.

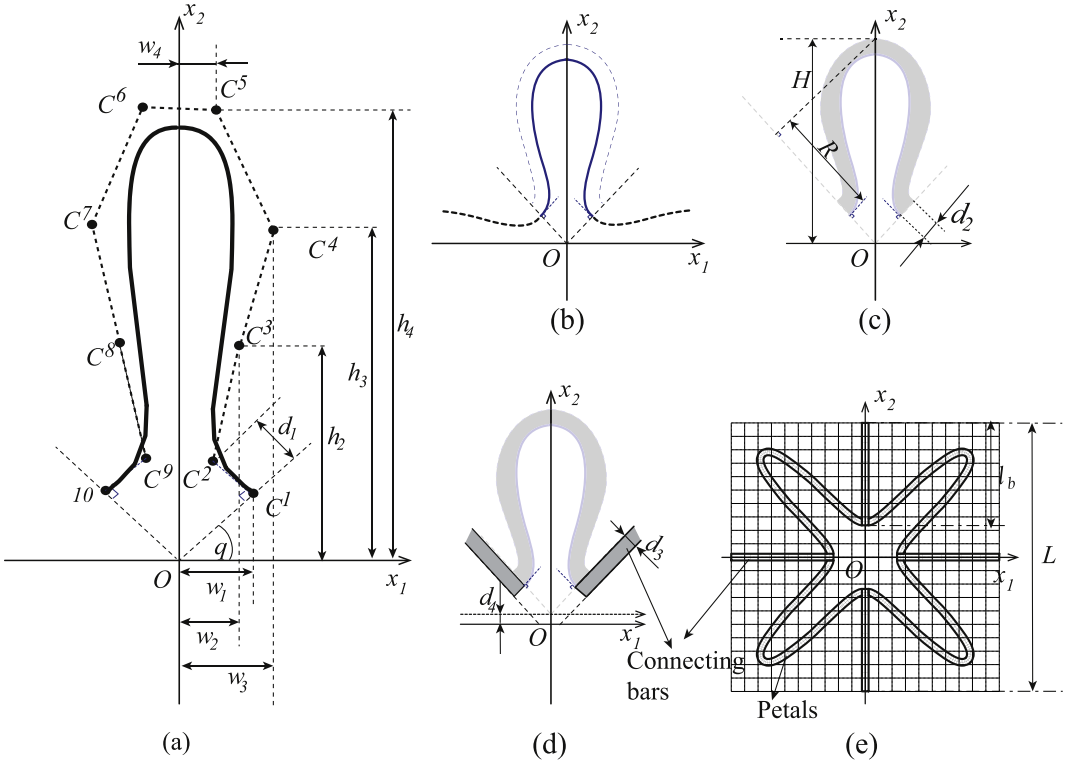

Fig. 2. Parameterization scheme for the tetra-petal-shaped auxetics: (a) interior petal boundary parameters, (b) exterior petal boundary generated by NURBS offsetting, (c) NURBS patch of a parent petal, and (d) connecting bars placement. The design in (e) corresponds to parameters of $w_1 = 1.5$, $w_2 = 1.0$, $w_3 = 1.0$, $w_4 = 0.5$, $h_4 = 10.25$, $d_1 = 0.5$, $d_2 = 0.5$, and $d_3 = 0.5$.

The additional parameters shown in Fig. 2 (c) and (e) are as follows: H is the petal height, R is the re-entrant depth and L is the side length of a unit cell. For convenience, the quantities R/H and H/L are termed *re-entrant ratio* and *petal size ratio*, respectively, hereinafter.

3.2. Deformation mechanism

The effective material properties of the tetra-petals auxetic can be evaluated using numerical homogenization method, which considers a square domain to be a representative volume element with the petals and bars as solid and the rest as void. To accommodate the curved features in tetra-petals auxetics, isogeometric analysis, which uses NURBS basis function as the shape functions to discretize the displacement field, is used as a tool for the numerical evaluation. The details about the numerical homogenization using isogeometric analysis for plane stress condition, including the strong and weak formulations of the corresponding boundary value problem, the isogeometric discretization scheme, and the multiple patches coupling method, can be found in the works of Refs.[1,2]. For convenience, the effective Poisson's ratio, Young's modulus and shear modulus are denoted as $\bar{\nu}$, $\bar{E}^Y$ and $\bar{G}$, respectively, hereinafter. Due to in-plane cubic symmetry of the considered periodic patterns, these three moduli entirely characterize the in-plane effective behavior of the architectured material.

Here, we consider a unit design with the following base parameter: $w_1 = 0.80$, $w_2 = 0.50$, $w_3 = 0.50$, $w_4 = 1.19$, $h_4 = 11.00$, $d_1 = 1.00$, $d_2 = 0.20$, and $d_3 = 0.20$. The influence of the various parameters on the underlying deformation mechanisms, and the resulting effect on the effective properties, are briefly summarized as follows:

- Influence of w_1 and w_2
  - The parameter analysis is performed by varying w_1 and w_2 simultaneously from 0.8 to 3. The sample tetra-petal structures in Fig. 3 (a) –(d) show that these two parameters control the opening of a petal. From Fig. 3, it is easily observed that as the petal opening increases, the auxeticity reduces significantly, with a marginal increase in stiffness and shear modulus. The underlying reason is that a bigger opening corresponds to a smaller re-entrant ratio, thus reducing the auxeticity and increasing the tensile and shear stiffness.
- Influence of w_3 and w_4
  - A smaller curvature (larger radius) increases the compliance of the structure. By increasing parameters w_3 and w_4 from 0.5 to 3 simultaneously, the curvature of the petals tips decreases monotonically, as depicted by the sample tetra-petals structures in Fig. 4. It is shown in Fig. 4 that as the tip curvature decreases, the effective Poisson's ratio increases while the effective tensile modulus decreases, with a negligible change of the shear modulus. When subjected to a tensile loading, the more compliant petal tip, induced by the smaller curvature, helps to "absorb" the corresponding deformation in the transverse direction. Compared to the influence of parameters w_1 and w_2, the negligible change of the shear modulus indicates that the shear modulus is highly dependent of the petal openings and almost independent of the petal curvature.
- Influence of the petal width d_2
  - The effective stiffness and the Poisson's ratio versus the petal width are plotted in Fig. 5. Both effective Poisson's ratio and Young's modulus increase significantly with petal width, with a marginal increase of the shear modulus. For a given curvature at the petal tip, the transverse deformation corresponding to a lateral tensile strain decreases with the structural stiffness. When the widths of the bars and petals are similar, the shear modulus is sensitive to the petal width change.

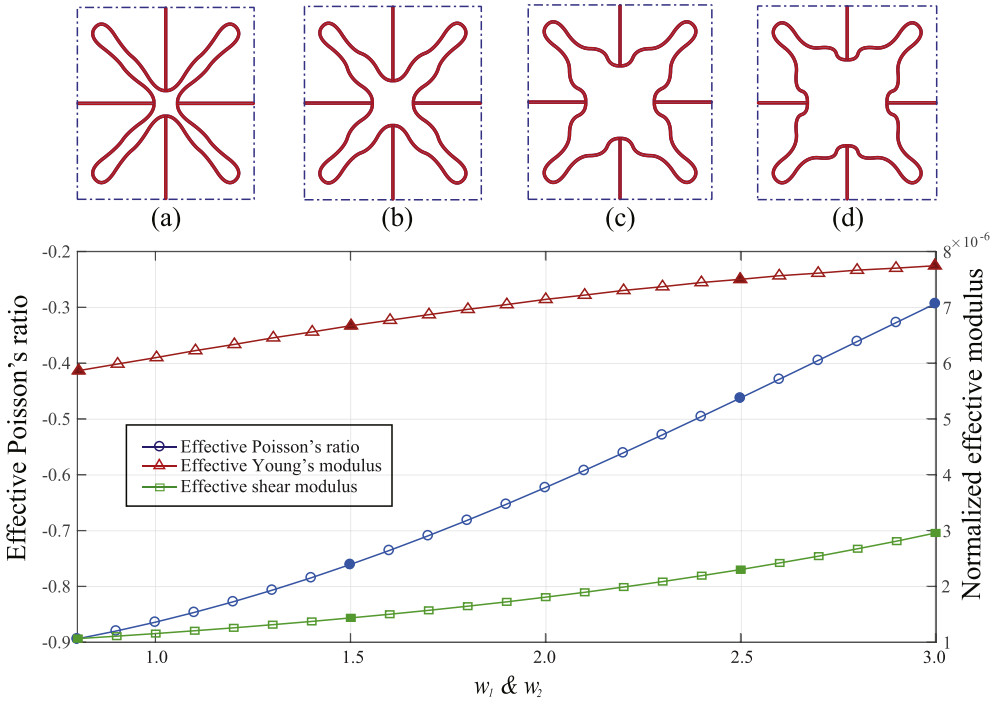

Fig. 3. Parameter analysis with respect to w_1 and w_2 that control the opening and re-entrant ratio of the petals. The solid symbols denote the effective properties for structures (a)–(d), corresponding to $w_1 = w_2 = 0.8, 1.5, 2.5$,and 3.0, respectively.

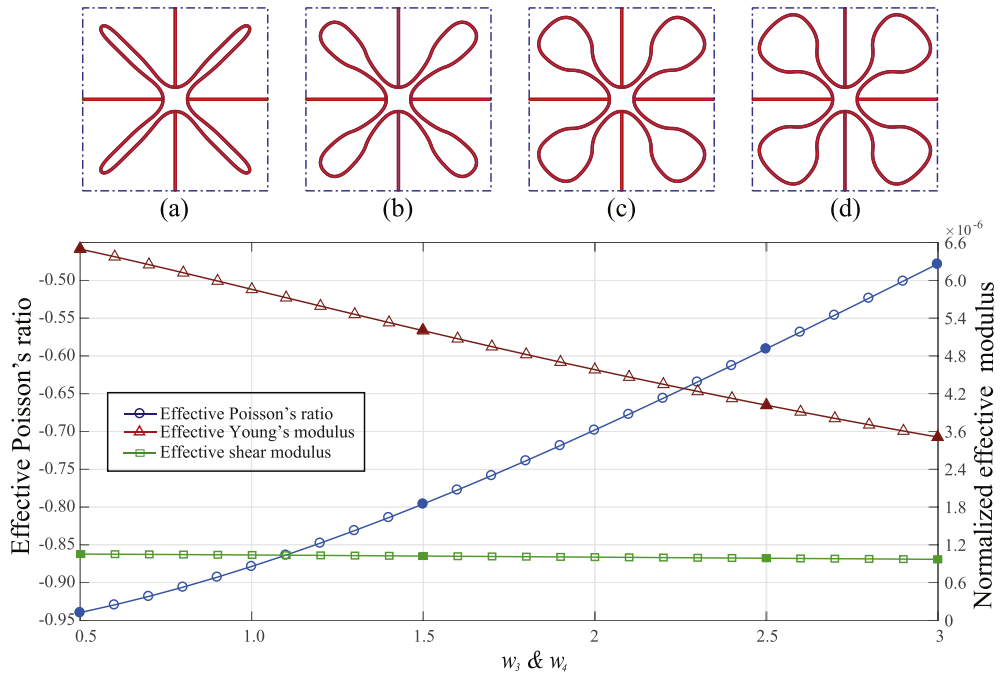

Fig. 4. Parameter analysis with respect to w_3 and w_4 that control the curvature of the petal tips. The solid symbols denote the effective properties for structures (a)–(d), corresponding to $w_3 = w_4 = 0.5, 1.5, 2.5$,and 3.0, respectively.

- Influence of the width of the connecting bars d_3
  - The effective stiffness and the Poisson's ratio versus the width of the connecting bars are plotted in Fig. 6. Note that the change in the connecting bar width results in a slight repositioning of the petal tips — see the overlay of two tetra-petals in Fig. 6. The slight change in the petal geometry induces a very small change in effective stiffness and Poisson's ratio, as depicted in Fig. 6. This suggests a negligible influence of the connecting bar width, departing from the observations for tri- and hexa-petals auxetics in Ref. [2]. Henceforth, the design parameter d_3 is not considered in this work for designing tetra-petals auxetics. For the shear modulus, a similar observation to the petal width d_2 is can be found, i.e., the shear modulus is sensitive to the bar width change only when the widths of the bars and petals are similar.

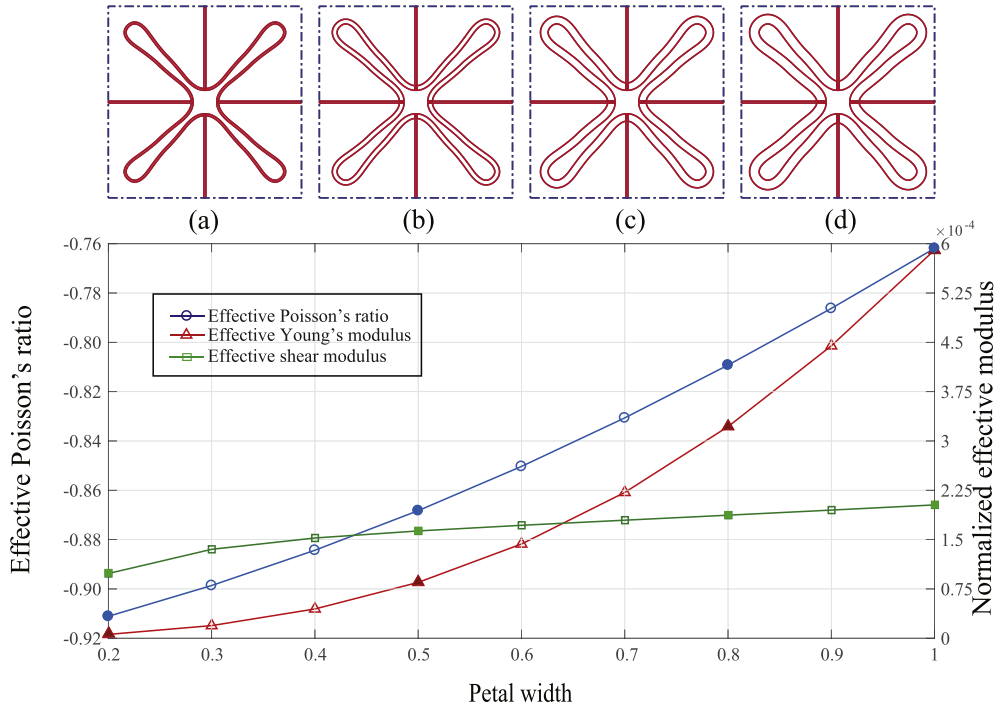

Fig. 5. Parameter analysis with respect to the petal width d_2. The solid symbols denote the effective properties for structures (a)–(d), corresponding to $d_2 = 0.2, 0.5, 0.8$,and 1.0, respectively.

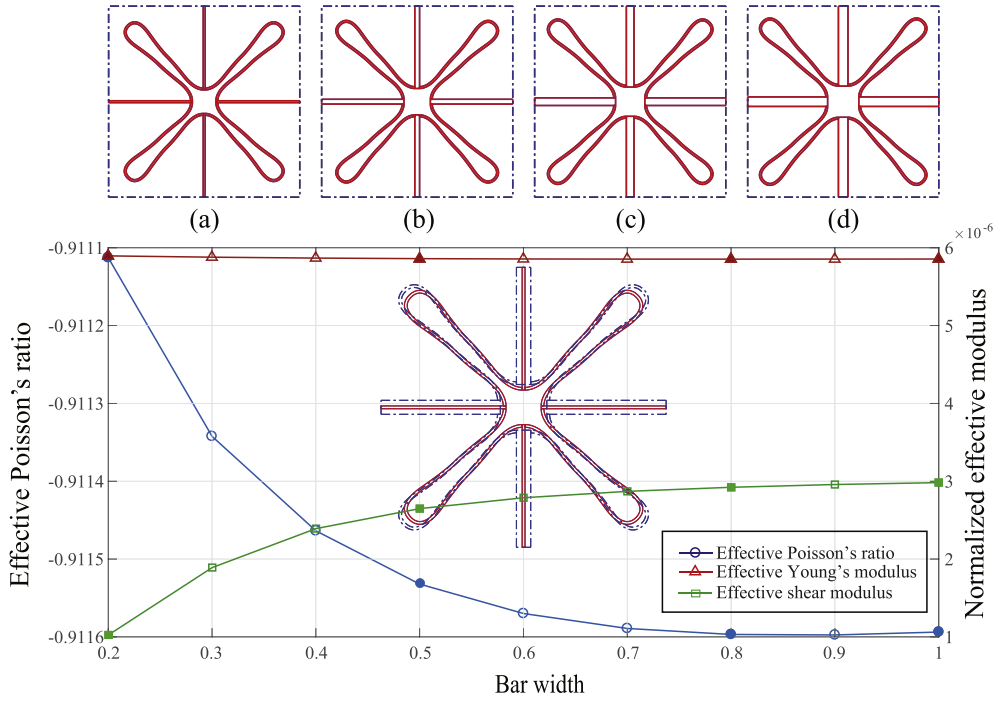

Fig. 6. Parameter analysis with respect to the width of the connecting bars d_3. The change of the effective NPR and the normalized effective Young's modulus is relatively small. The solid symbols denote the effective properties for structures (a)–(d), corresponding to $d_3 = 0.2, 0.5, 0.8$,and 1.0, respectively. The overlay of (a) and (d) shown in the graph depicts a slight change in petal tip positioning.

- Influence of petal size ratio H/L
  - The petal size ratio, H/L, also affects the effective auxetic performance. This is studied by increasing the unit size, i.e. the side length L, from 20 to 40, while keeping other parameters the same. The effective properties versus length L are plotted in Fig. 7. It shows that by increasing the length L (decreasing the petal size ratio), the effective Young's

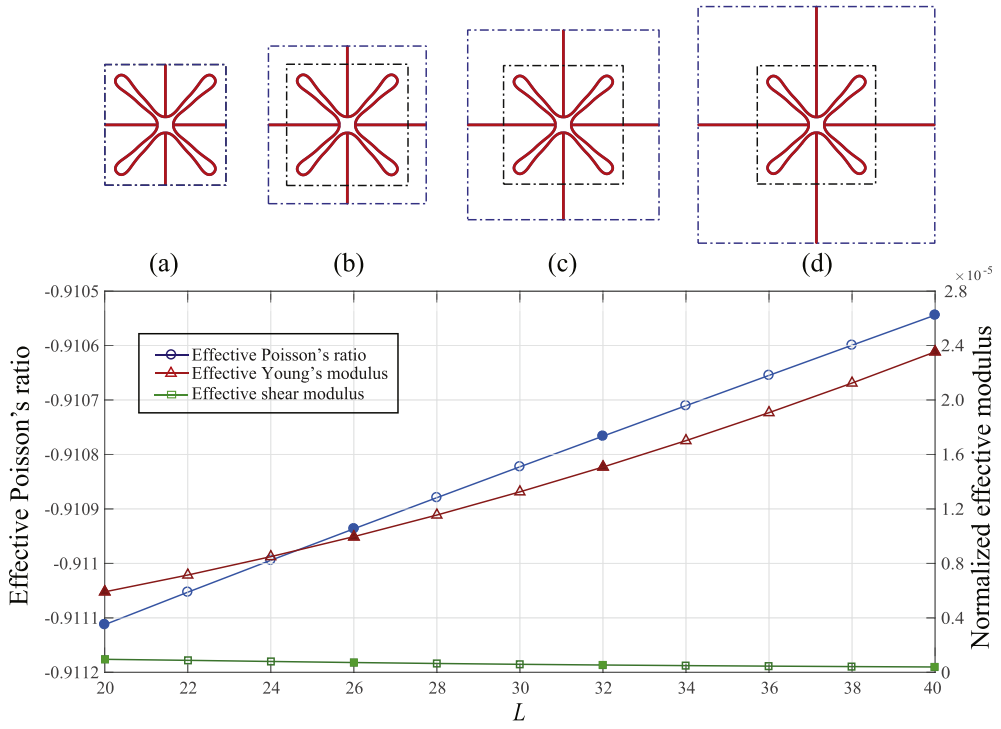

Fig. 7. Parameter analysis with respect to the unit side length L that is inversely proportional to the petal size ratio (H/L). The decrement of the effective NPR is relatively small. The solid symbols denote the effective properties for structures (a)–(d), corresponding to $L = 20, 26, 32$,and 40, respectively.

modulus increases significantly, with a negligible change of the effective shear modulus and Poisson's ratio, which indicates that a negligible influence of the connecting bar length, (or the petal size ratio) on the auxetic performance.

We note that some of the deformation mechanisms discussed here draw parallels with those for the reference star-shaped auxetics, e.g., on the re-entrant ratio, petal (star) and connecting bar widths. Other mechanisms related to the curvature of petal tips are distinct features of the tetra-petals structures. It is not the intention of this section to elaborate on the deformation mechanisms underlying a tetra-petals structure. Rather, it is to briefly highlight the extent of influence on the effective properties for the various geometrical parameters, at times leading to conflicting overall trends (e.g., Figs. 4 and 5). It is emphasized that while a deformation mechanism associated with a geometrical feature can be easily identified, it is not a straight forward task to establish a general relationship between all geometrical parameters and the resulting overall effective Young's modulus, shear modulus and Poisson's ratio. To facilitate the design of tetra-petals with targeted effective properties, a systematic optimization framework is thus provided below.

4. Design bounding graphs for different stiffness constraints

4.1. Design optimization framework

The problem statement is to design an auxetic structure with tunable Poisson's ratios at a given stiffness. As shown in Section 3.2, the width parameter d_3 of the connecting bars has a negligible influence on the effective properties. Hence, in this work, we use the same width for petals and connecting bars, i.e., $d_2 = d_3$. Eventually, the design problem is to find a set of optimal values for the design variables $\boldsymbol{\chi} = [w_1, w_2, w_3, w_4, h_4, d_1, d_2]$ such that a cost function is minimized with constraints satisfied. For a tunable target material property design framework, the objective function can be set as

$$\min \quad \Phi[\boldsymbol{\chi}] := (\bar{\nu} - \check{\nu})^2, \tag{1}$$

subjected to

$$\begin{cases} \Psi_Y[\boldsymbol{\chi}] := \bar{E}^Y - \check{E}^Y = 0 \\ \Psi_S[\boldsymbol{\chi}] := \bar{G} - \check{G} = 0 \end{cases} \tag{2}$$

The quantity $\check{\nu}$ in the objective function Φ is a target Poisson's ratio, $\check{E}^Y$ in the design constraint Ψ_Y is the given effective Young's modulus, and $\check{G}$ in the design constraint Ψ_S is the given effective shear modulus. The constraints Ψ_Y and Ψ_S may exist together at the same time or separately depending on the design requirements. The optimization problem may be formulated as

$$\begin{cases} \text{find} \quad \tilde{\chi}_i \in [\underline{\chi}_i, \quad \bar{\chi}_i], \quad i = 1, \quad 2, \cdots, \quad \text{such that} \\ \Phi[\tilde{\boldsymbol{\chi}}] \le \Phi[\boldsymbol{\chi}], \quad \Psi_Y[\tilde{\boldsymbol{\chi}}] = 0, \quad \Psi_S[\tilde{\boldsymbol{\chi}}] = 0, \qquad \forall \tilde{\chi}_i \in [\underline{\chi}_i, \quad \bar{\chi}_i], \end{cases} \tag{3}$$

where $\underline{\chi}_i$ and $\bar{\chi}_i$ are the lower and upper bounds of χ_i, respectively.

4.2. Design optimization setting

In the optimization studies, it is essential to set upper and lower bounds for the design variables such that the solutions are feasible and meaningful, e.g., the size of the petals should not be too big to overlap with other parts; the relative width of the components should not be too small to cause significant manufacturing difficulty; the curvature of the curved parts should not be too big to introduce high stress concentrations. For the problems shown in this paper, the upper and lower bounds for the design variables $w_{1,2,3,4}$ are set to be $[3, 3, 3, 1]$ and $[0.8, 0.5, 0.5, 0.25]$, respectively, to avoid overlaps between the petals and connecting bars. The upper and lower bounds for design variable h_4 are set to be 13.5 and 7, respectively, such that the petals are small enough to fit within a unit cell, and yet of a sufficient size to generate a relatively large curvature at the vertices. Referring to Fig. 2 (a), the upper bound of the offsetting variable d_1 is set to be 1, such that a reasonable gap exists between the two arms of the petal, and the lower bound is set to be 0.3 such that a minimal distance is maintained between control points C^1 and C^2. For the petal and connecting bar widths d_2 and d_3, the upper bound is set as 1 to control the parametrization modeling. To account for a possible minimum thickness constraint in the manufacturing process, the lower bound for d_2 and d_3 is set as 0.2.

A unit cell has an area of 400, with the initial design depicted in Fig. 2 (e). The initial design has an effective Poisson's ratio of $\bar{\nu} = -0.67$ and effective Young's modulus $\bar{E}^Y = 1.24 \times 10^{-4} E_0^Y$ for plane stress condition, and $\bar{\nu} = -0.58$ and $\bar{E}^Y = 9.55 \times 10^{-4} E_0^Y$ for plane strain condition. The quantity E_0^Y is the Young's modulus of the base material.

4.3. Bounding graphs of auxetic limits with different stiffness constraints

It should be noted that a target effective property may not be achievable for the presented design framework. Hence, it is useful to have bounding graphs indicating the limiting Poisson's ratio with different stiffness constraints, e.g., the graphs shown in Ref. [16]. By setting a target value of $\check{\nu} = -1$ for the effective Poisson's ratio in the objective function Φ in Eq. (1), a solution is obtained with the lowest achievable Poisson's ratio, i.e., the design limit of the auxeticity. To accommodate the possible application mentioned in Section 1, the analysis are done in both plane stress and plane strain conditions.

For simplicity, the bounding graphs obtained here only consider the constraints of different effective Young's moduli. The constraint of shear modulus can be included based on practical requirements, which is elaborated with design studies with tunable effective properties in Section 5. The design optimization study is implemented sequentially over a range values of $\check{E}^Y$ to generate the design limit curves in Fig. 8. The optimized designs corresponding to each data point in Fig. 8 are depicted in Fig. 9 for both plane stress and plane strain conditions. The optimal design parameters for the optimal solutions are listed in Table 1.

The bounding graphs depicted in Fig. 8 can be used as a guide on the effective properties that can be obtained from these tetra-petals auxetics. This information can be helpful for designing novel functional structures with programmable local properties, e.g., the novel lattice structures presented in Refs. [47-49].

4.4. Discussion

From Figs. 8 and 9 and Table 1, it is observed that the optimal solutions of the plane stress and plane strain conditions for each stiffness constraint are similar. Stationary points at the stiffness of $\frac{\bar{E}^Y}{E_0^Y} = 8 \times 10^{-6}$ are obtained with the lowest attainable Poisson's ratio at cases A3 and B3. Away from the stationary point with a higher/lower effective stiffness, the auxeticity of the petal-shaped structures reduces.

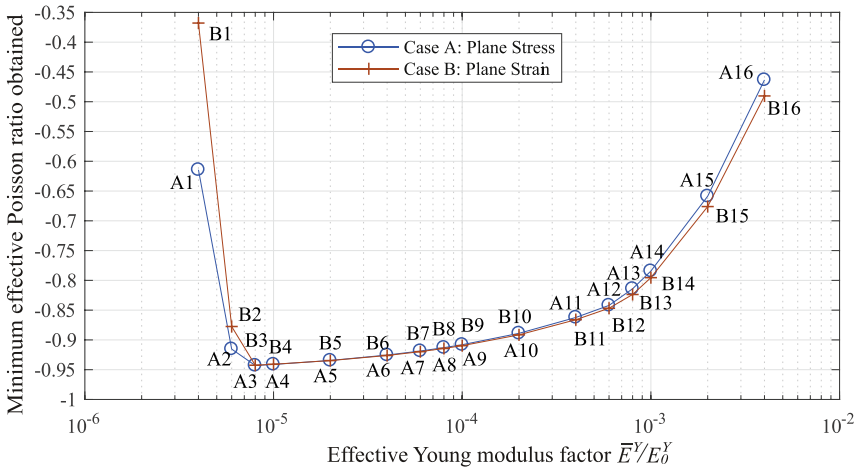

Fig. 8. Design bounding graphs of the minimum achievable Poisson's ratio for the tetra-petals auxetic structures. The results based on the plane stress formulation are relatively close to those based on plane strain formulation.

The optimal results in Fig. 9 and Table 1 conform to the mechanisms discussed in Section 3.2:

- For all optimal designs, the design parameter w_1 reaches its lower bound to obtain good auxetic performance with maximum re-entrant ratio; so does the parameter w_2 except for case B1;
- The optimal parameters of cases A1 and A2 are identical, except parameters w_3 and w_4 which control the curvature of the petals tips. Compared to case A2, case A1 has a much smaller curvature, which helps to increase the compliance of the structure to eventually form a softer auxetic;
- As the stiffness constraint increases, the petal size ratio H/L decreases and the petal width increases. The increase in stiffness is achieved at the expense of auxeticity;
- A lower stiffness of the tetra-petals structure can be achieved either by reducing the part width, or by changing the petal shape. Once the minimum width is reached, the petal shape becomes the dominant factor;

5. Tunable designs, potential applications, numerical verifications and effective anisotropy

5.1. Design with tunable effective properties

As a demonstration of the framework presented in Section 4.1, design studies are carried out for both plane stress and plane strain conditions to obtain effective Poisson's ratios of: (a) $\check{\nu} = -0.75$; (b) $\check{\nu} = -0.5$; and (c) $\check{\nu} = -0.25$; subjected to a Young's modulus constraint $\bar{E}^Y = 4.0 \times 10^{-4} E_0^Y$ and a shear modulus constraint $\bar{G} = 1.0 \times 10^{-4} E_0^Y$. The designs obtained are depicted in Fig. 10, with an exact match of the target material properties. The optimized design parameters for these cases are listed in Table 2. Such designs with tunable effective properties help to provide the necessary freedom

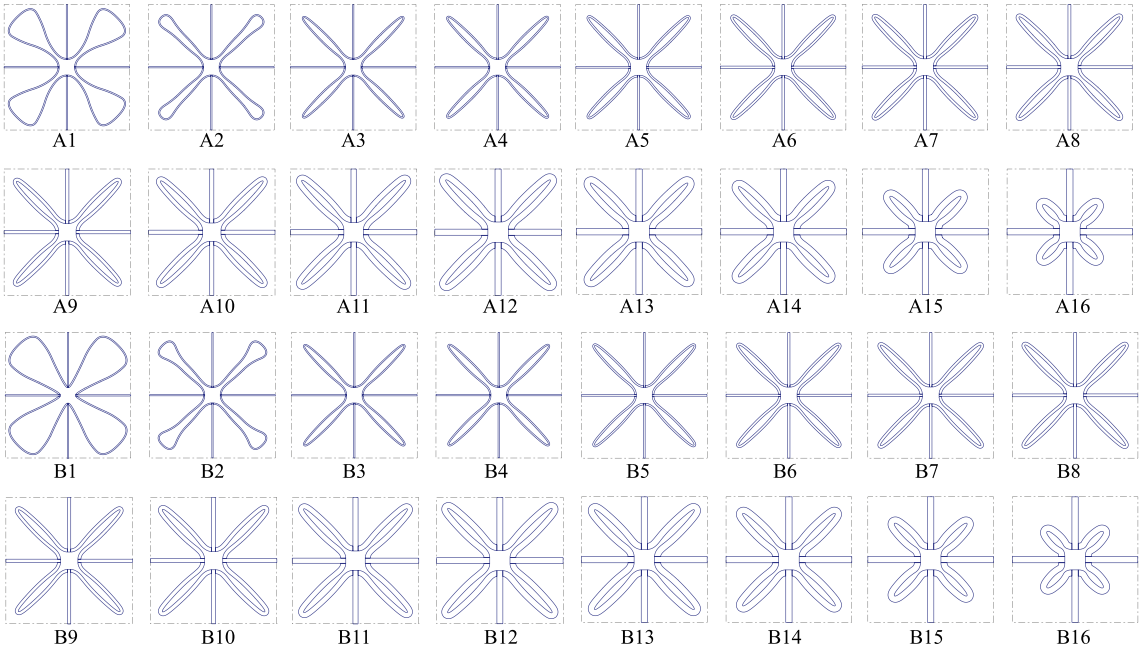

Fig. 9. Optimal solutions of the tetra-petals structures for cases with stiffness constraints indicated in Fig. 8.

Table 1
The optimal design parameters and the volume fraction of each optimized solution in Fig. 8.

Cases	Design variables $\chi = [w_1, w_2, w_3, w_4, h_4, d_1, d_2]$	Volume fraction (%)
A1	[0.80, 0.50, 2.17, 3.00, 11.00, 1.00, 0.20]	0.07
A2	[0.80, 0.50, 0.50, 1.19, 11.00, 1.00, 0.20]	0.06
A3	[0.80, 0.50, 0.50, 0.25, 11.00, 1.00, 0.21]	0.06
A4	[0.80, 0.50, 0.50, 0.25, 11.00, 1.00, 0.23]	0.07
A5	[0.80, 0.50, 0.50, 0.25, 11.00, 1.00, 0.29]	0.09
A6	[0.80, 0.50, 0.50, 0.25, 11.00, 1.00, 0.37]	0.11
A7	[0.80, 0.50, 0.50, 0.25, 11.00, 1.00, 0.42]	0.13
A8	[0.80, 0.50, 0.50, 0.25, 11.00, 1.00, 0.47]	0.14
A9	[0.80, 0.50, 0.50, 0.25, 11.00, 1.00, 0.51]	0.15
A10	[0.80, 0.50, 0.50, 0.25, 11.00, 1.00, 0.65]	0.19
A11	[0.80, 0.50, 0.50, 0.25, 11.00, 1.00, 0.83]	0.25
A12	[0.80, 0.50, 0.50, 0.25, 11.00, 1.00, 0.97]	0.29
A13	[0.80, 0.50, 0.50, 0.25, 10.25, 1.00, 1.00]	0.28
A14	[0.80, 0.50, 0.50, 0.25, 9.44, 1.00, 1.00]	0.27
A15	[0.80, 0.50, 0.50, 0.25, 7.25, 1.00, 1.00]	0.23
A16	[0.80, 0.50, 0.50, 0.25, 5.43, 1.00, 1.00]	0.19
B1	[0.80, 1.64, 2.92, 3.00, 11.00, 0.30, 0.20]	0.07
B2	[0.80, 0.50, 0.50, 1.86, 11.00, 1.00, 0.20]	0.06
B3	[0.80, 0.50, 0.50, 0.25, 11.00, 1.00, 0.20]	0.06
B4	[0.80, 0.50, 0.50, 0.25, 11.00, 1.00, 0.22]	0.07
B5	[0.80, 0.50, 0.50, 0.25, 11.00, 1.00, 0.28]	0.08
B6	[0.80, 0.50, 0.50, 0.25, 11.00, 1.00, 0.36]	0.11
B7	[0.80, 0.50, 0.50, 0.25, 11.00, 1.00, 0.41]	0.12
B8	[0.80, 0.50, 0.50, 0.25, 11.00, 1.00, 0.45]	0.14
B9	[0.80, 0.50, 0.50, 0.25, 11.00, 1.00, 0.49]	0.15
B10	[0.80, 0.50, 0.50, 0.25, 11.00, 1.00, 0.63]	0.19
B11	[0.80, 0.50, 0.50, 0.25, 11.00, 1.00, 0.81]	0.24
B12	[0.80, 0.50, 0.50, 0.25, 11.00, 1.00, 0.94]	0.28
B13	[0.80, 0.50, 0.50, 0.25, 10.51, 1.00, 1.00]	0.29
B14	[0.80, 0.50, 0.50, 0.25, 9.68, 1.00, 1.00]	0.27
B15	[0.80, 0.50, 0.50, 0.25, 7.45, 1.00, 1.00]	0.23
B16	[0.80, 0.50, 0.50, 0.25, 5.61, 1.00, 1.00]	0.19

for designing novel functionally graded structures, such as e-skins with tunable local properties.

5.2. Functionally graded structures made with tetra-petals auxetics

It was demonstrated in the previous section that tetra-petals auxetics can be designed to have the same stiffnesses, with different effective Poisson's ratios. This facilitates design of functionally

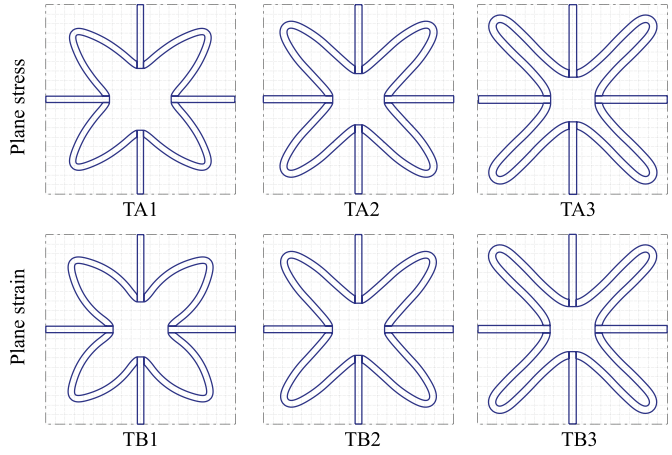

Fig. 10. Tunable material property designs with different target Poisson's ratios of −0.75 (TA1 and TB1), −0.50 (TA2 and TB2) and −0.25 (TA3 and TB3), respectively, with TA1–3 for plane stress cases and TB1–3 for plane strain cases. The depicted designs match the target Poisson's ratios exactly with the same normalized Young's modulus of $\bar{E}^Y = 4.0 \times 10^{-4} E_0^Y$ and shear modulus of $\bar{G} = 1.0 \times 10^{-4} E_0^Y$.

Table 2
The optimal design parameters and the volume fraction of each optimized solution in Fig. 10, with TA1–3 for plane stress cases and TB1–3 for plane strain cases.

Cases	Design variables $\chi = [w_1, w_2, w_3, w_4, h_4, d_1, d_2]$	Volume fraction (%)
TA1	[2.07, 1.73, 1.28, 0.31, 9.09, 0.30, 0.67]	0.15
TA2	[1.66, 1.29, 1.20, 0.47, 9.96, 0.32, 0.74]	0.19
TA3	[1.38, 0.60, 0.70, 0.57, 10.76, 0.73, 0.80]	0.22
TB1	[1.81, 1.93, 1.57, 0.34, 9.25, 0.35, 0.68]	0.16
TB2	[1.70, 1.29, 1.20, 0.47, 9.97, 0.31, 0.71]	0.18
TB3	[1.41, 0.60, 0.72, 0.58, 10.78, 0.74, 0.77]	0.21

graded structures with tunable local material properties. To demonstrate this potential application, we adopt the design cases of TA1–3 to build a lattice structure shown in Fig. 11 (a), with a uniform bar width of 0.77. The deformed shape in tensile loading is shown in Fig. 11 (b). It is clear that the functionally graded structure exhibits a variable vertical expansion at different locations, which can be utilized for the design of shape matching structures shown in Ref. [47].

5.3. Numerical verifications using ABAQUS and auxeticity in nonlinear deformation regime

The isogeometric analysis codes used to design the tetra-auxetic structures had been verified in multiple ways before performing the design studies in this work. However, to make sure that the designs presented are correct, numerical verifications using the commercial finite element software ABAQUS are carried out for case TB3 shown in Fig. 10. The unit cell is firstly saved into a format based on Initial Graphics Exchange Specification (IGES) and subsequently imported into ABAQUS with the same material property used for design. Tensile and pure shear loadings are applied to the plane strain mesh separately to compute the effective Poisson's ratio and elastic modulus, as depicted in Fig. 12 (a) and (b), respectively. The results match with the IGA solutions well. A compression loading case is also performed with the same NPR computed as the tension loading case, which indicates that in the linear elastic regime, the effective Poisson's ratio are identical in tension and compression.

The deformation mechanisms of the tetra-petals in tension and compression are also briefly illustrated here. The tetra-petals in Fig. 13 (a) is subjected to tensile and compressive loadings with geometrical nonlinearity considerations. In the linear elastic regime, the effective Poisson's ratio is identical in tension and compression, as shown in Fig. 13 (e). Beyond a deformation limit into the large deformation regime, however, the auxeticity of the tetra-petals differ significantly in tension and compression. In tension, the re-entrant ratio in the loading direction decreases, as shown in Fig. 13 (b). The resulting auxeticity thus reduces with tensile deformation, similar to the observations in Fig. 3. In compression, the converse is true, where the re-entrant ratio increases with deformation, as shown in Fig. 13 (c). Accordingly, the auxeticity increases with compressive deformation. However, the petal arms come into contact with one another at a compressive deformation threshold, which hinder the deformation mechanism underlying the auxeticity effect. The effective Poisson's ratio in Fig. 13 (f) thus increases rapidly in compression once the self-contact between petals is established. A further compressive loading leads to an inter-petal contact between neighboring units, see the limiting point in Fig. 13 (d) where the petals touch the boundaries of the unit cell. Note that the deformation mechanisms highlighted in this section pertains to the large deformation regime, which is

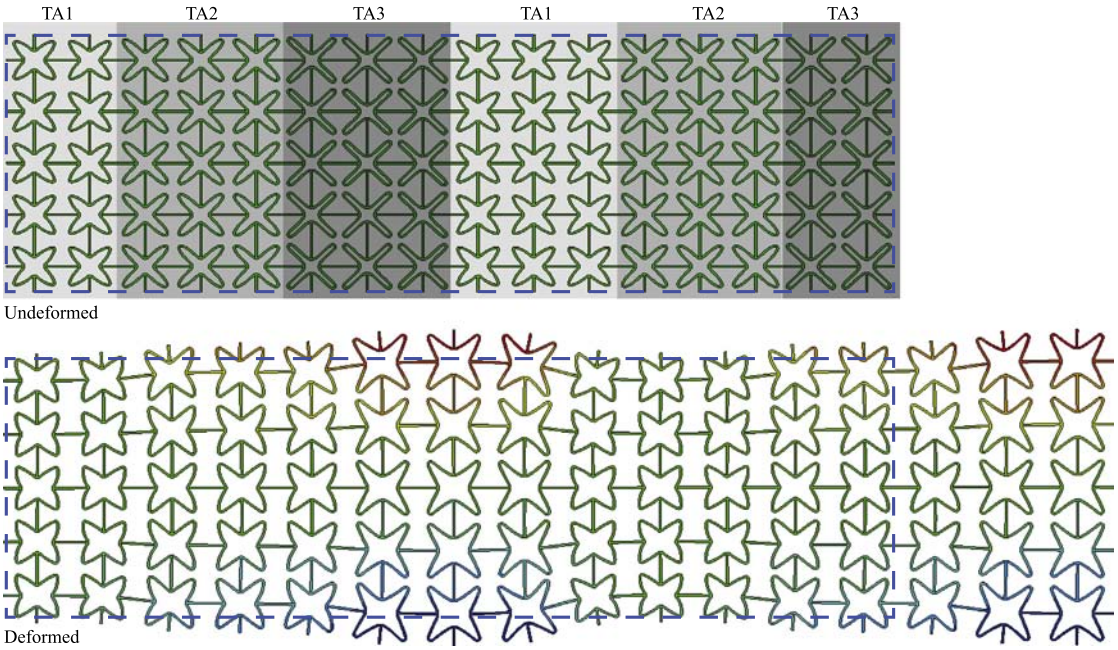

Fig. 11. A functionally graded structure built from unit structures of TA1, TA2 and TA3. The blue dash rectangular describes the region of the undeformed structure. The deformation is scaled by a factor of 5. The structure exhibits a variable vertical expansion at different locations under tensile deformation, which can be utilized for the design of shape matching structures, e.g., in Ref. [47]. (For interpretation of the references to color in this figure legend, the reader is referred to the web version of this article.)

beyond the scope of the presented framework. Its extension to the large deformation regime will be the focus of future work.

5.4. Anisotropic effective behavior

It should be noted that the effective material properties of tetra-petals auxetics are in-plane anisotropic — a feature that is not commonly discussed in the literature of architecture materials. Depending on the types of applications, this behavior can be interesting (e.g. in sensor systems where variable deformation are required along different directions) or undesirable (e.g. in a support system providing resistance against different loading directions). To illustrate this, the effective properties are evaluated along different directions for cases TB1–3, which are depicted as polar plots in Fig. 14 to give the following observations.

- Fig. 14 (a) shows a wide region around 0° and 90° with strongly negative Poisson ratio, with a narrow band around ±45° where auxeticity vanishes.
- With respect to the reference vertical and horizontal directions, Fig. 14 (b) shows that the effective Young's modulus can reduce by 2.6 times at ±45°. In contrast, the effective shear modulus in Fig. 14 (c) is significantly higher at ±45°.

This example clearly illustrates a significant anisotropic effect of tetra-petals auxetics. For applications concerned with targeted directional responses, additional constraints involving effective properties in different directions can easily be incorporated into the presented optimization framework.

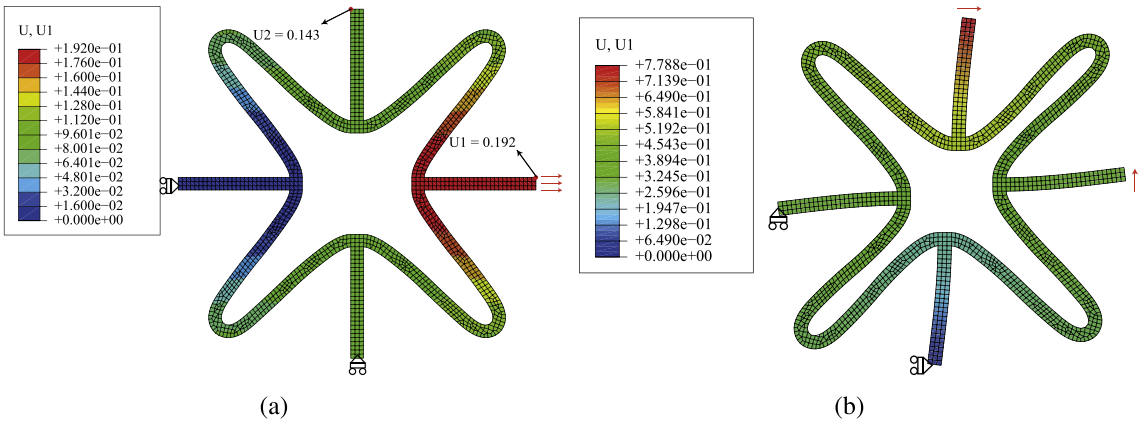

Fig. 12. (a) Tensile loading with left and bottom roller constrained. Traction loaded at the right end is 7.72×10^{-5} (the bar width is 0.772 and distributed traction is 1.0×10^{-4}), leading to a effective stress of $7.72 \times 10^{-5}/20$ and effective strains of $E_{11} = 0.192/20$; $E_{22} = 0.143/20$, which corresponds to a effective tensile modulus of 4.01×10^{-4} and a effective Poisson ratio of −0.7448, matching the design model computed using IGA. (b) Pure shear loading case with same magnitude of shear traction, leading to a effective shear stress of $7.72 \times 10^{-5}/20$ and shear strain of $E_{12} = 0.7788/20$, which corresponds to a shear modulus of 0.99×10^{-4}, matching the IGA solution.

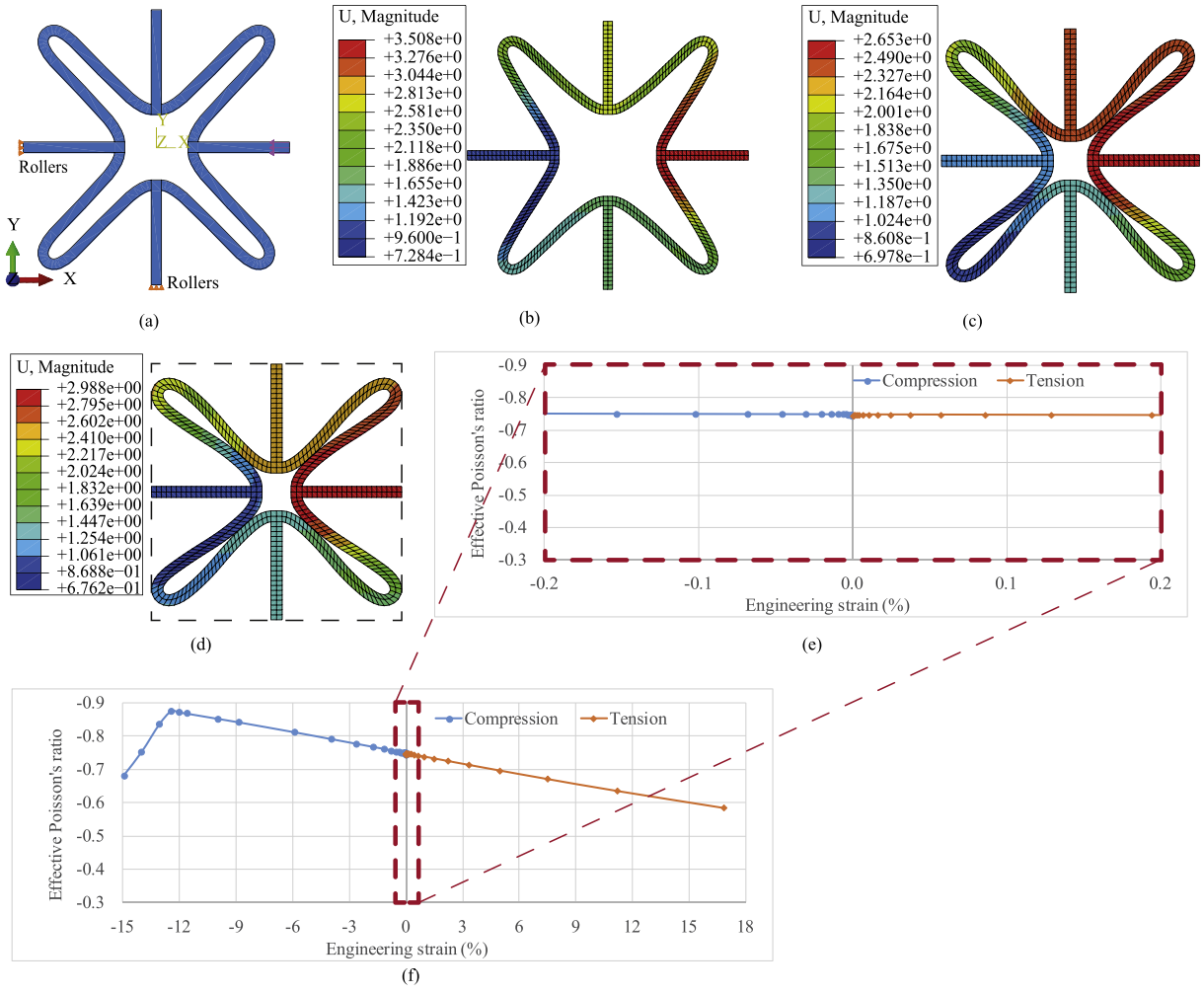

Fig. 13. Compression and tension loadings for design case TB3 under plane strain condition with geometrical nonlinearity effects. (a) Boundary conditions setting: left end with x-direction fixed; lower end with y-direction fixed; right end with compression/tension load; and upper end free. (b) The tension deformation stage with a strain of 16.83%. (c) Deformed geometry with compression strain of −12.43% where petal self-contact occurs. (d) The compression deformation stage with a strain of −14.9% where inter-contact between neighboring units occurs. Effective Poisson's ratio in the (e) small and (f) large deformation regime.

6. Experiments

6.1. Out-of-plane buckling for thin samples

For re-entrant structures that are thin in out-of-plane direction, buckling can develop in tension loading, as demonstrated in Fig. 15 (a). This draws caution to results obtained using plane stress formulations for such thin structures. Importantly, the out of plane buckling should be treated for practical applications. For wearable electronic devices, this problem can be resolved with an extra membrane layer coating on the auxetic structure and sticking to skin, as implemented in Refs.[3,5]. For thick structures designed based on

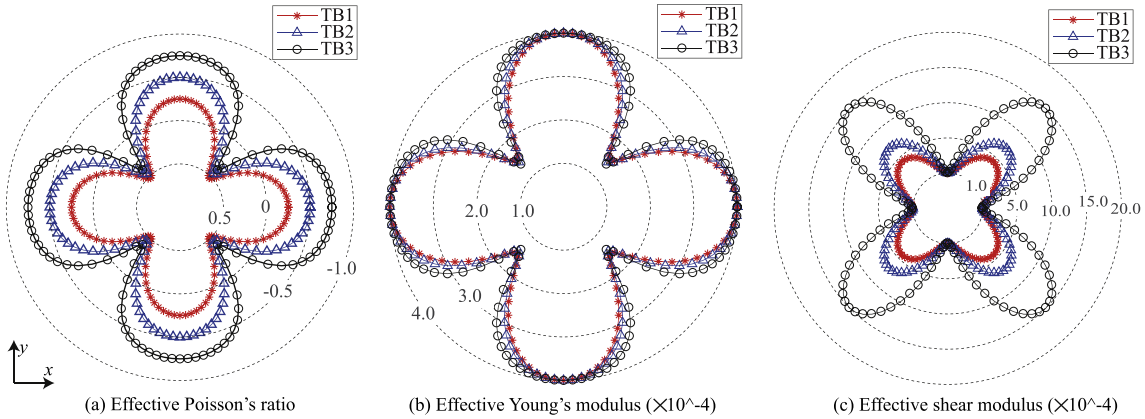

Fig. 14. Effective (a) Poisson's ratios, (b) Young's moduli and (c) shear moduli along different directions for design cases TB1, TB2 and TB3.

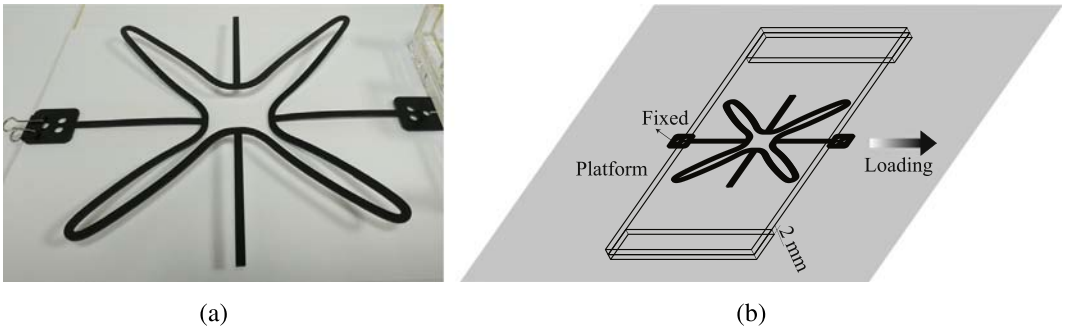

Fig. 15. (a) Out-of-plane buckling under tension of unit sample A9. (b) Testing platform for the unit samples.

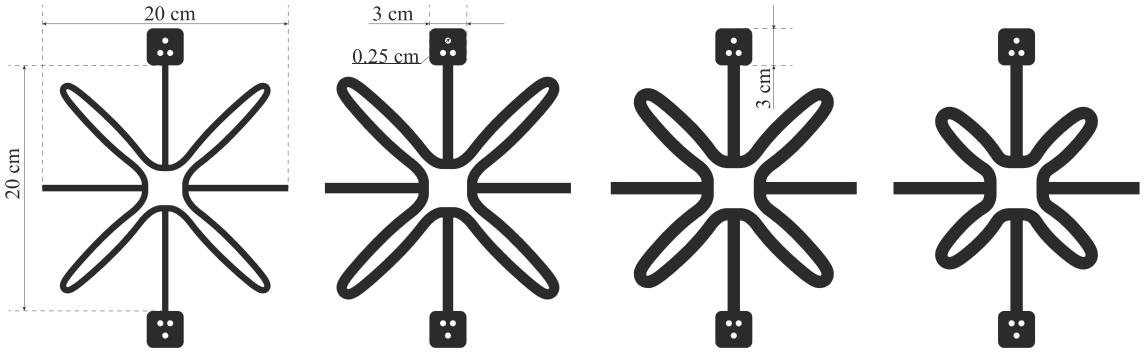

Fig. 16. Unit samples of cases A9, A11, A14 and A15 with a dimension of 20 × 20 cm.

plane strain formulations with thick out-of-plane dimensions, the out-of-plane buckling is not a problem.

6.2. Experimental verifications

To verify the effective properties, numerical cases A9, A11, A14 and A15 shown in Figs. 8 and 9 are fabricated using laser cutting technology. The sample units have a dimension of 20 × 20 cm, as shown in Fig. 16. The material used for these samples is Acrylonitrile Butadiene Styrene (ABS) with a Young's modulus about 2.3 GPa and a Poisson's ratio about 0.3. The thickness of a sample is about 1.6 mm.

The samples are placed on a platform shown in Fig. 15 (b) with one end fixed and the other end loaded such that a unit structure deform with a strain between 3% and 5 %. To avoid out of plane buckling of the samples in tension (see Fig. 15 (a)) that leads to a "softer" material, a transparent acrylic plate is placed on the top of the samples. The gap between the acrylic plate and the platform is

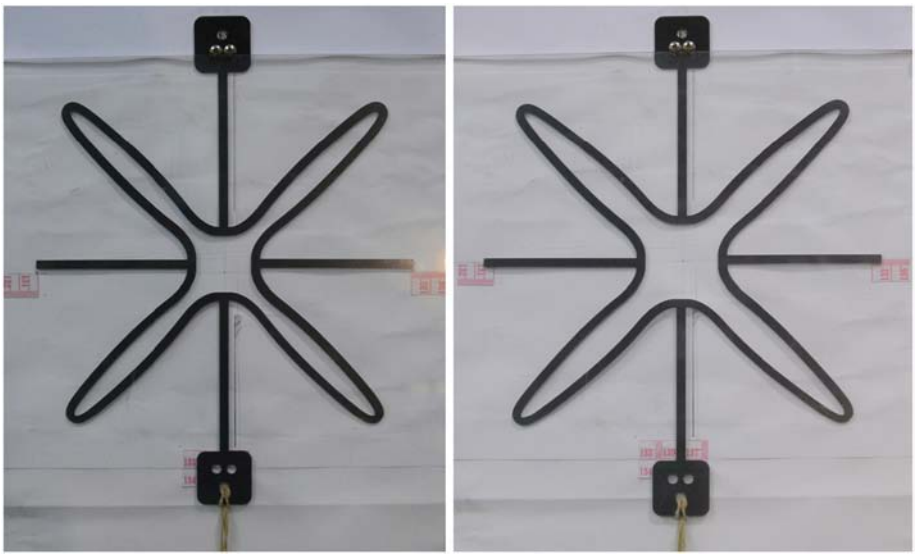

Fig. 17. A unit sample (case A9) before (left) and after (right) tension loading. The in-plane bar/petal width is 5.1 mm, much larger than the out-of-plane thickness of 1.6 mm, which is a key factor of the out-of-plane buckling under tension.

Table 3
The numerical effective Poisson's ratio (PR) and the tested results for the unit samples.

Sample	Numerical	Tested PR			Error
ID	PR	Loading 1	Loading 2	Average	
A9	−0.908	−0.885	−0.892	−0.889	2.15%
A11	−0.862	−0.841	−0.861	−0.851	1.33%
A14	−0.782	−0.755	−0.760	−0.758	3.07%
A15	−0.665	−0.632	−0.637	−0.635	4.51%

Table 4
The normalized effective Young's moduli (YM) and the tested results for the unit samples.

Sample	Numerical	Tested YM			Error
ID	YM	Loading 1	Loading 2	Average	
A9	2.3×10^{-4}	2.067×10^{-4}	2.2×10^{-4}	2.133×10^{-4}	7.25%
A11	9.2×10^{-4}	9.730×10^{-4}	9.459×10^{-4}	9.595×10^{-4}	4.29%
A14	23×10^{-4}	22.667×10^{-4}	22.000×10^{-4}	22.333×10^{-4}	2.90%
A15	46×10^{-4}	46.759×10^{-4}	45.833×10^{-4}	46.292×10^{-4}	0.64%

about 2 mm. This means that the out-of-plane displacement of the specimen, if any, would be about 0.4 mm. The 0.4 mm gap provides sufficient space to prevent a significant friction influence and an out-of-plane displacement that is too big, to significantly affect the measured property. The tension experiment of a unit of design case A9 is depicted in Fig. 17.

The tested results of the effective Poisson's ratios of the four samples are presented in Table 3, which match the numerical predictions very well. The tested results of the effective Young's modulus are presented in Table 4, showing a good agreement between the numerical simulations and the experimental results. Note that the error between the numerical and experimental results of the Young's modulus decreases as the effective stiffness increases. This is because the re-entrant feature leads to an out of plane buckling, as depicted in Fig. 15 (a), which occurs more easily with a lower effective stiffness (softer design).

To further verify the effective Poisson's ratio, another experimental test is carried out using a lattice sample for design case A14, as depicted in Fig. 18. The sample is placed on a platform with one end fixed and the other end stretched such that the structure deforms with a strain of 3.33%. The orthogonal strain is 2.52%, corresponding to an effective NPR of −0.758. The error between the numerical and experimental results is 3.31%, indicating a good match. The results here also suggest that the sample unit cell experiment can characterize the effective properties sufficiently.

7. Conclusions

In this work, we seek to provide a systematic design study for tetra-petal auxetics. To deal with the curved features of the petal-shaped auxetics, NURBS parameterization and isogeometric analysis are adopted to achieve a seamless transition between design and analysis models. Using numerical homogenization method, the mechanism of the tetra-petals auxetics is studied based on sequential parameter analysis. By understanding the mechanism, design studies using structural optimization technique are performed to obtain bounding graphs of the minimum achievable Poisson's ratio subjected to different stiffness constraints for both plane stress and plane strain conditions. The bounding graphs can be used as a guide to design innovative structures with programmable local properties. Design studies with tunable effective material properties are performed and a potential application of functionally graded structure made from these designs is presented. Finally, numerical and experimental verifications are performed to verify the isogeometric design results.

The tetra-petals auxetics studied in this work have a relatively large design space in terms of petal form and size modification, to achieve a wide range of effective Young's modulus and negative Poisson's ratio. The almost independence of the connecting bar size facilitates the design of functionally graded structures with tunable local performances. Finally, the anisotropy of tetra-petals auxetics is

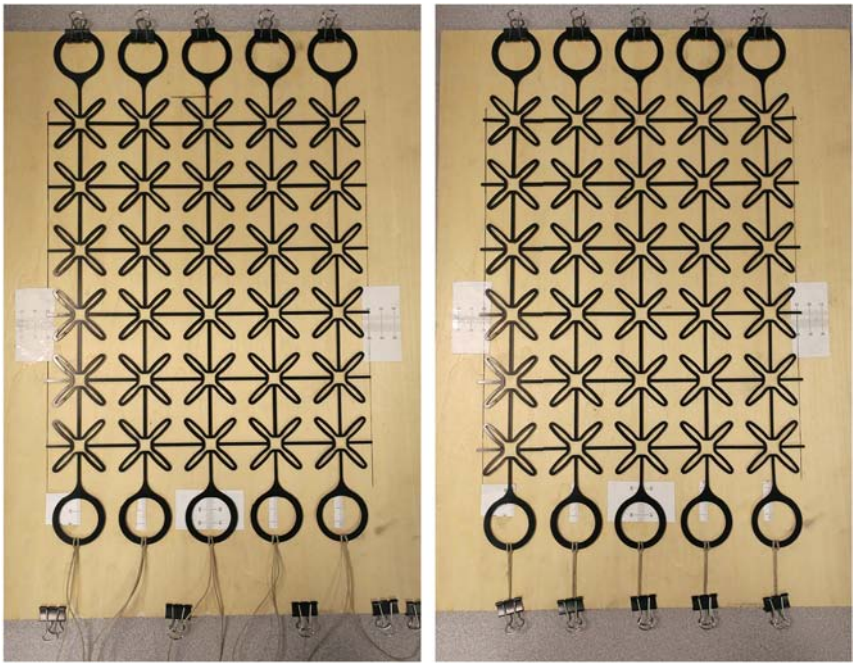

Fig. 18. Testing platform: the initial (left) and the loaded (right) states of a lattice sample with design case A14.

highlighted — a topic which is not commonly discussed in the literature of architecture materials. To achieve targeted directional behavior, additional constraints involving effective properties in different directions can be incorporated into the presented framework.

CRediT authorship contribution statement

Zhen-Pei Wang: Conceptualization, Formal analysis, Writing - original draft. **Leong Hien Poh:** Conceptualization, Supervision. **Yilin Zhu:** Formal analysis, Writing - review & editing. **Justin Dirrenberger:** Conceptualization, Writing - review & editing. **Samuel Forest:** Conceptualization, Writing - review & editing.

Acknowledgments

ZP Wang, LH Poh and Y Zhu acknowledge the financial support from Ministry of Education - Singapore (MOE) Tier 2 Grant R302000139112. Y Zhu also acknowledge the financial support from National Natural Science Foundation of China (11702036).

References

[1] Z.-P. Wang, L.H. Poh, J. Dirrenberger, Y. Zhu, S. Forest, Isogeometric shape optimization of smoothed petal auxetic structures via computational periodic homogenization, Computer Methods in Applied Mechanics and Engineering 323 (2017) 250–271.
[2] Z.-P. Wang, L.H. Poh, Optimal form and size characterization of planar isotropic petal-shaped auxetics with tunable effective properties using IGA, Composite Structures 201 (2018) 486–502. ISSN 0263-8223.
[3] K.-I. Jang, H.U. Chung, S. Xu, C.H. Lee, H. Luan, J. Jeong, H. Cheng, G.-T. Kim, S.Y. Han, J.W. Lee, et al. Soft network composite materials with deterministic and bio-inspired designs, Nature Communications 6 (2015)
[4] Q. Ma, H. Cheng, K.-I. Jang, H. Luan, K.-C. Hwang, J.A. Rogers, Y. Huang, Y. Zhang, A nonlinear mechanics model of bio-inspired hierarchical lattice materials consisting of horseshoe microstructures, Journal of the Mechanics and Physics of Solids 90 (2016) 179–202.
[5] Y. Jiang, Z. Liu, N. Matsuhisa, D. Qi, W.R. Leow, H. Yang, J. Yu, G. Chen, Y. Liu, C. Wan, Auxetic mechanical metamaterials to enhance sensitivity of stretchable strain sensors, Advanced Materials 30 (12) (2018) 1706589.
[6] X. Ren, R. Das, P. Tran, T.D. Ngo, Y.M. Xie, Auxetic metamaterials and structures: a review, Smart Materials and Structures (2018)
[7] R.F. Almgren, An isotropic three-dimensional structure with Poisson's ratio–1, Journal of Elasticity 15 (4) (1985) 427–430.
[8] P. Theocaris, G. Stavroulakis, P. Panagiotopoulos, Negative Poisson's ratios in composites with star-shaped inclusions: a numerical homogenization approach, Archive of Applied Mechanics 67 (4) (1997) 274–286.
[9] M. Shokri Rad, Z. Ahmad, A. Alias, Computational approach in formulating mechanical characteristics of 3D star honeycomb auxetic structure, Advances in Materials Science and Engineering 2015 (2015)
[10] D. Prall, R. Lakes, Properties of a chiral honeycomb with a Poisson's ratio of −1, International Journal of Mechanical Sciences 39 (3) (1997) 305–314.
[11] Y. Zhu, Z.-P. Wang, L.H. Poh, Auxetic hexachiral structures with wavy ligaments for large elasto-plastic deformation, Smart Materials and Structures 27 (5) (2018) 055001.
[12] H. Ebrahimi, D. Mousanezhad, H. Nayeb-Hashemi, J. Norato, A. Vaziri, 3D cellular metamaterials with planar anti-chiral topology, Materials & Design 145 (2018) 226–231.
[13] H. Zong, H. Zhang, Y. Wang, M.Y. Wang, J.Y. Fuh, On two-step design of microstructure with desired Poisson's ratio for AM, Materials & Design 159 (2018) 90–102.
[14] I. Masters, K. Evans, Models for the elastic deformation of honeycombs, Composite Structures 35 (4) (1996) 403–422.
[15] J. Xiong, D. Gu, H. Chen, D. Dai, Q. Shi, Structural optimization of re-entrant negative Poisson's ratio structure fabricated by selective laser melting, Materials & Design 120 (2017) 307–316.
[16] T. Wang, L. Wang, Z. Ma, G.M. Hulbert, Elastic analysis of auxetic cellular structure consisting of re-entrant hexagonal cells using a strain-based expansion homogenization method, Materials & Design 160 (2018) 284–293.
[17] J.N. Grima, K.E. Evans, Auxetic behavior from rotating squares, Journal of Materials Science Letters 19 (17) (2000) 1563–1565.
[18] J. Dagdelen, J. Montoya, M. de Jong, K. Persson, Computational prediction of new auxetic materials, Nature Communications 8 (1) (2017) 323.
[19] L. Mizzi, E. Mahdi, K. Titov, R. Gatt, D. Attard, K.E. Evans, J.N. Grima, J.-C. Tan, Mechanical metamaterials with star-shaped pores exhibiting negative and zero Poisson's ratio, Materials & Design 146 (2018) 28–37.
[20] S. Babaee, J. Shim, J.C. Weaver, E.R. Chen, N. Patel, K. Bertoldi, 3D Soft metamaterials with negative Poisson's ratio, Advanced Materials 25 (36) (2013) 5044–5049.
[21] X. Ren, J. Shen, P. Tran, T.D. Ngo, Y.M. Xie, Design and characterisation of a tuneable 3D buckling-induced auxetic metamaterial, Materials & Design 139 (2018) 336–342.
[22] Y. He, Y. Zhou, Z. Liu, K. Liew, Pattern transformation of single-material and composite periodic cellular structures, Materials & Design 132 (2017) 375–384.
[23] Y. Prawoto, Seeing auxetic materials from the mechanics point of view: a structural review on the negative Poisson's ratio, Computational Materials Science 58 (2012) 140–153.
[24] K.K. Saxena, R. Das, E.P. Calius, Three decades of auxetics research — materials with negative Poisson's ratio: a review, Advanced Engineering Materials 18 (11) (2016) 1847–1870.
[25] X. Ren, J. Shen, P. Tran, T.D. Ngo, Y.M. Xie, Auxetic nail: design and experimental study, Composite Structures 184 (2018) 288–298.
[26] X. Ren, J. Shen, A. Ghaedizadeh, H. Tian, Y.M. Xie, A simple auxetic tubular structure with tuneable mechanical properties, Smart Materials and Structures 25 (6) (2016) 065012.
[27] A. Ingrole, A. Hao, R. Liang, Design and modeling of auxetic and hybrid honeycomb structures for in-plane property enhancement, Materials & Design 117 (2017) 72–83.
[28] Q. Gao, X. Zhao, C. Wang, L. Wang, Z. Ma, Multi-objective crashworthiness optimization for an auxetic cylindrical structure under axial impact loading, Materials & Design 143 (2018) 120–130.
[29] T. Li, Y. Chen, X. Hu, Y. Li, L. Wang, Exploiting negative Poisson's ratio to design 3D-printed composites with enhanced mechanical properties, Materials & Design 142 (2018) 247–258.
[30] M. Kucewicz, P. Baranowski, J. Małachowski, A. Popławski, P. Płatek, Modelling, and characterization of 3D printed cellular structures, Materials & Design 142 (2018) 177–189.
[31] O. Sigmund, Materials with prescribed constitutive parameters: an inverse homogenization problem, International Journal of Solids and Structures 31 (17) (1994) 2313–2329.
[32] L. Xia, P. Breitkopf, Design of materials using topology optimization and energy-based homogenization approach in Matlab, Structural and Multidisciplinary Optimization 52 (6) (2015) 1229–1241.
[33] F. Wang, Systematic design of 3D auxetic lattice materials with programmable Poisson's ratio for finite strains, Journal of the Mechanics and Physics of Solids 114 (2018) 303–318.
[34] J. Schwerdtfeger, F. Wein, G. Leugering, R. Singer, C. Körner, M. Stingl, F. Schury, Design of auxetic structures via mathematical optimization, Advanced Materials 23 (22-23) (2011) 2650–2654.
[35] J. Ganghoffer, I. Goda, A. Novotny, R. Rahouadj, J. Sokolowski, Homogenized couple stress model of optimal auxetic microstructures computed by topology optimization, ZAMM-Journal of Applied Mathematics and Mechanics/Zeitschrift für Angewandte Mathematik und Mechanik (2017)
[36] S. Czarnecki, T. Łukasiak, T. Lewiński, The isotropic and cubic material designs. Recovery of the underlying microstructures appearing in the least compliant continuum bodies, Materials 10 (10) (2017) 1137.
[37] T. Strek, H. Jopek, E. Idczak, K.W. Wojciechowski, Computational modelling of structures with non-intuitive behaviour, Materials 10 (12) (2017) 1386.
[38] H. Zhang, Y. Luo, Z. Kang, Bi-material microstructural design of chiral auxetic metamaterials using topology optimization, Composite Structures 195 (2018) 232–248.
[39] A. Clausen, F. Wang, J.S. Jensen, O. Sigmund, J.A. Lewis, Topology optimized architectures with programmable Poisson's ratio over large deformations, Advanced Materials 27 (37) (2015) 5523–5527.
[40] C. Wang, S. Xia, X. Wang, X. Qian, Isogeometric shape optimization on triangulations, Computer Methods in Applied Mechanics and Engineering 331 (2018) 585–622.
[41] Y. Wang, Z.-P. Wang, Z. Xia, L.H. Poh, Structural design optimization using isogeometric analysis: a comprehensive review, Computer Modeling in Engineering & Sciences (2018)
[42] V. Braibant, C. Fleury, Shape optimal design using B-splines, Computer Methods in Applied Mechanics and Engineering 44 (3) (1984) 247–267.
[43] W.H. Zhang, D. Wang, J.-G. Yang, A parametric mapping method for curve shape optimization on 3D panel structures, International Journal for Numerical Methods in Engineering 84 (4) (2010) 485–504.
[44] D. Wang, W.-H. Zhang, A bispace parameterization method for shape optimization of thin-walled curved shell structures with openings, International Journal for Numerical Methods in Engineering 90 (13) (2012) 1598–1617.
[45] S. Turteltaub, Functionally graded materials for prescribed field evolution, Computer Methods in Applied Mechanics and Engineering 191 (21-22) (2002) 2283–2296.
[46] S. Turteltaub, Optimal control and optimization of functionally graded materials for thermomechanical processes, International Journal of Solids and Structures 39 (12) (2002) 3175–3197.
[47] M.J. Mirzaali, S. Janbaz, M. Strano, L. Vergani, A.A. Zadpoor, Shape-matching soft mechanical metamaterials, Nature, Scientific Reports 8 (2018) 1–7.
[48] Y. Wang, H. Xu, D. Pasini, Multiscale isogeometric topology optimization for lattice materials, Computer Methods in Applied Mechanics and Engineering 316 (2017) 568–585.
[49] Y. Han, W. Lu, Evolutionary design of nonuniform cellular structures with optimized Poisson's ratio distribution, Materials & Design 141 (2018) 384–394.
[50] H. Niknam, A. Akbarzadeh, D. Rodrigue, D. Therriault, Architected multi-directional functionally graded cellular plates, Materials & Design 148 (2018) 188–202.

[51] M.M. Abdalla, S. Setoodeh, Z. Gürdal, Design of variable stiffness composite panels for maximum fundamental frequency using lamination parameters, Composite structures 81 (2) (2007) 283–291.
[52] J. Dirrenberger, S. Forest, D. Jeulin, Elastoplasticity of auxetic materials, Computational Materials Science 64 (2012) 57–61.
[53] J. Dirrenberger, S. Forest, D. Jeulin, Effective elastic properties of auxetic microstructures: anisotropy and structural applications, International Journal of Mechanics and Materials in Design 9 (1) (2013) 21–33.
[54] L. Xia, P. Breitkopf, Recent advances on topology optimization of multiscale nonlinear structures, Archives of Computational Methods in Engineering 24 (2) (2017) 227–249.
[55] D. Da, J. Yvonnet, L. Xia, M.V. Le, G. Li, Topology optimization of periodic lattice structures taking into account strain gradient, Computers & Structures 210 (2018) 28–40.
[56] D. Wang, M.M. Abdalla, W. Zhang, Buckling optimization design of curved stiffeners for grid-stiffened composite structures, Composite Structures 159 (2017) 656–666.
[57] D. Wang, M.M. Abdalla, W. Zhang, Sensitivity analysis for optimization design of non-uniform curved grid-stiffened composite (NCGC) structures, Composite Structures 193 (2018) 224–236.
[58] D. Wang, M.M. Abdalla, Z.-P. Wang, Z. Su, Streamline stiffener path optimization (SSPO) for embedded stiffener layout design of non-uniform curved grid-stiffened composite (NCGC) structures, Computer Methods in Applied Mechanics and Engineering 191 (21-22) (2018) 2283–2296.
[59] Z. Ding, O. Weeger, H.J. Qi, M.L. Dunn, 4D rods: 3D structures via programmable 1D composite rods, Materials & Design 137 (2018) 256–265.
[60] Z. Wu, L. Xia, S. Wang, T. Shi, Topology optimization of hierarchical lattice structures with substructuring, Computer Methods in Applied Mechanics and Engineering 345 (2019) 602–617. ISSN 0045-7825.
[61] H.M. Kolken, A. Zadpoor, Auxetic mechanical metamaterials, RSC Advances 7 (9) (2017) 5111–5129.
[62] K.K. Yang, J.H. Zhu, C. Wang, D.S. Jia, L.L. Song, W.H. Zhang, Experimental validation of 3D printed material behaviors and their influence on the structural topology design, Computational Mechanics 61 (5) (2018) 581–598.
[63] B. Caddock, K. Evans, Microporous materials with negative Poisson's ratios. I. Microstructure and mechanical properties, Journal of Physics D: Applied Physics 22 (12) (1989) 1877.
[64] J.N. Grima, R. Gatt, A. Alderson, K. Evans, On the potential of connected stars as auxetic systems, Molecular Simulation 31 (13) (2005) 925–935.
[65] G.W. Milton, Composite materials with Poisson's ratios close to −1, Journal of the Mechanics and Physics of Solids 40 (5) (1992) 1105–1137.